Applied Thermal Engineering 281 (2025) 128689

Contents lists available at ScienceDirect

Applied Thermal Engineering

journal homepage: www.elsevier.com/locate/apthermeng

Research Paper

Coolant flow in structured grinding wheels: CFD validation via high-speed imaging and particle tracking

Sharlane Costa [a,b,c], Andrews Souza [a,c,d], Lucas Neves [c,d,e], João Ribeiro [c,*], Mário Pereira [f], Delfim Soares [a,b]

[a] CMEMS - Center for MicroElectromechanical, University of Minho, 4800-058 Guimarães, Portugal
[b] LABBELS – Associate Laboratory, Braga/Guimarães, Portugal
[c] Centro de Investigação de Montanha (CIMO), Instituto Politécnico de Bragança, Campus S. Apolónia, 5300-253 Bragança, Portugal
[d] MEtRICs, Mechanical Eng. Dep., Univ. of Minho, Campus de Azurém, Guimarães, Portugal
[e] International Iberian Nanotechnology Laboratory, Braga 4715-330, Portugal
[f] Centro de Física das Universidades do Minho e do Porto, Braga, Portugal

ARTICLE INFO

Keywords:
CFD validation
Particle tracking
High-speed imaging analysis
Grinding wheel
Internal cooling channels
Grinding performance improvement

ABSTRACT

Efficient coolant delivery is essential in grinding to control heat generation, minimize tool wear, and preserve workpiece integrity. However, Computational Fluid Dynamics (CFD) models commonly used for coolant system design remain rarely validated due to the extreme speeds and complex multiphase flows involved. This work addresses this gap by combining CFD simulations with targeted experiments to evaluate heat removal effectiveness in internally cooled grinding wheels with three channel inclinations: positive, straight, and negative. Transparent resin prototypes enabled high-speed imaging and particle tracking for flow field validation, while grinding tests measured temperature rise and mechanical loads. Results demonstrate that channel inclination strongly affects fluid acceleration, jet coherence, and penetration into the grinding zone, with the positive inclination producing the highest outlet velocities and reducing temperature rise by up to 67%. Particle tracking confirmed CFD predictions within 16% deviation, validating the model's reliability. By establishing a direct correlation between coolant jet dynamics, heat dissipation, and process performance, this study demonstrates a methodology for the thermal optimization of internal cooling systems in rotating tools. The approach provides a pathway for improving energy efficiency, extending tool life, and reducing coolant consumption in industrial machining processes.

1. Introduction

Grinding is the most common method for machining of materials like ceramics, composites, alloys and super alloys having high strength to weight ratio [1,2]. Despite its versatility and ability to achieve high dimensional accuracy in such demanding materials, the process is also characterized by intense heat generation in the cutting zone, which makes coolant delivery a critical factor for maintaining performance and avoiding thermal damage [3–5].

Grinding is intrinsically associated with high thermal loads in the workpiece, since nearly all the mechanical energy supplied is converted into heat at the grinding zone. This heat transfer to the surface layer can cause severe thermal damage, including burn, phase transformations, hardness reduction, and tensile residual stresses. In extreme cases, it may also lead to cracks and surface oxidation, compromising part integrity and limiting productivity. The extent of thermal damage is closely linked to the heat partition ratio into the workpiece, which depends on grinding parameters and determines whether the generated energy will be dissipated through the chips, grinding wheel, fluid, or retained in the material [6,7]. High-performance grinding processes are especially prone to excessive temperature rise, with surface interface temperatures exceeding 800 °C under unfavorable conditions, leading to accelerated wheel wear and deterioration of workpiece quality. Consequently, accurate thermal control of the grinding zone has become a central focus in research, as optimizing heat transfer is a prerequisite not only for process reliability but also for sustainable and productive grinding operations [8].

Efficient coolant delivery plays a decisive role in the performance

* Corresponding author.
E-mail address: jribeiro@ipb.pt (J. Ribeiro).

https://doi.org/10.1016/j.applthermaleng.2025.128689
Received 24 August 2025; Received in revised form 2 October 2025; Accepted 9 October 2025
Available online 11 October 2025

and reliability of grinding processes [9–11]. By controlling the temperature in the contact zone, reducing friction between the abrasive grains and the workpiece, and flushing away chips, coolant contributes directly to dimensional accuracy, surface integrity, and tool life [12–14]. However, in conventional external cooling systems, the coolant jet must overcome the aerodynamic barrier generated by the rotating wheel. At elevated peripheral speeds, this air layer can deflect or fragment the fluid jet, substantially reducing the volume and velocity of coolant that reaches the grinding interface [15–19]. As a result, inadequate cooling often leads to excessive heat generation, thermal damage to the workpiece, accelerated wheel wear, and unstable process performance [20,21].

To overcome these limitations, internal coolant delivery systems have been proposed, in which fluid is fed directly into the grinding wheel and discharged through dedicated channels distributed along its periphery [22–24]. This configuration allows the coolant to bypass the air barrier and be delivered directly to the grinding zone, improving penetration, heat dissipation, and lubrication efficiency [25]. Several studies have demonstrated that structured grinding wheels with internal channels can significantly lower grinding temperatures and forces, thereby enhancing process efficiency and stability [26,27]. Nevertheless, the effectiveness of such systems depends strongly on the design of the internal channels, which not only govern fluid acceleration, jet orientation, and distribution at the outlet, but also determine how the coolant interacts with the air barrier and reaches the workpiece surface [28]. Previous studies have systematically examined parameters such as channel diameter [29], number of channels [30], inclination angle [31], and multi-layer arrangements [28], revealing their influence on flow rate, jet penetration, and overall cooling efficiency.

More broadly, the application method itself has a decisive influence on the thermal and tribological performance of grinding operations [32]. Conventional flood cooling, although widely used, often suffers from low penetration into the contact zone at high wheel speeds, limiting heat removal and lubrication efficiency [33]. Alternative strategies such as minimum quantity lubrication (MQL) [34] and cryogenic cooling [35] have shown potential to significantly reduce grinding temperature, tangential and normal forces, and surface roughness. Comparative studies indicate that internal coolant delivery generally provides superior penetration into the grinding zone and more stable process behavior than purely external systems, especially under high-speed conditions [29,36]. Beyond technical performance, coolant application strategies must also address environmental and economic considerations, as conventional flood systems consume large volumes of cutting fluid, generating substantial procurement, maintenance, and disposal costs, while posing risks to operator health and contributing to environmental contamination [37–39].

Within this consolidated technological framework, recent advances in computational fluid dynamics (CFD) have expanded the possibilities for analyzing and optimizing coolant delivery in grinding operations [40,41]. Numerical simulations allow detailed visualization of flow fields inside complex geometries, quantifying parameters such as velocity distribution, pressure gradients, and turbulence intensity that are difficult to measure experimentally. Yu et al. [42] used this approach to analyze the hydrodynamics of the fluid in the grinding zone and explain how the bionic structures of the grinding wheel help to break the air barrier created by rotation, increasing the efficiency of lubrication and cooling. Thekkoot Surendran and Sooraj [43] applied similar simulations to study airflow around both conventional and segmented wheels, correlating segmentation patterns with boundary layer characteristics, coolant penetration, and thermal performance, and identifying an optimal number of segments for improved cooling in wet grinding conditions.

In the context of internally cooled grinding wheels, CFD has been applied to study the influence of channel geometry, inclination, and outlet configuration on fluid acceleration and jet coherence. For example, Peng et al. [25] conducted simulations to optimize the outlets in a directional internal-cooling grooved grinding wheel, aiming to increase outlet flow rate, improve distribution uniformity, and enhance coolant delivery efficiency under different supply pressures before manufacturing the tool. Zhao et al. [44] modeled multiphase flow in a porous self-lubricating internal-cooling grinding wheel, aiming to evaluate how porosity and different concentrations of nanofluids influence velocity distribution, jet trajectories, and cooling performance prior to manufacturing and experimental testing. Wang et al. [45] analyzed the internal flow behavior, enabling the prediction of velocity distribution and coolant coverage to guide design adjustments prior to fabrication and performance testing.

Although CFD is widely used to analyze coolant flow in both conventional and internally cooled grinding wheels, its experimental validation remains rare due to the harsh and dynamic nature of the grinding environment. High rotational speeds generate strong air barriers and complex multiphase interactions between coolant, air, and debris, making direct measurement inside the wheel or at the contact zone extremely difficult. Optical methods, such as high-speed imaging, are limited by restricted access, small field of view, and distortions caused by spray and reflections. Reproducing the exact conditions in simulations also demands precise geometry, material properties, and boundary conditions, including turbulence levels and internal flow distribution. These challenges, combined with the small size of internal channels and transient flow behavior, make quantitative validation of CFD predictions particularly challenging.

High-speed imaging and particle tracking are well-established techniques in fields such as biomedical engineering, where they are extensively used to analyze blood flow, cell transport, and microfluidic behavior with high spatial and temporal resolution [46–48]. These methods allow precise quantification of flow velocity, trajectory, and interaction with complex geometries, providing valuable insights for both research and clinical applications [49]. However, despite their proven capability in capturing transient and small-scale fluid phenomena, their application in grinding processes remains virtually unexplored. The high rotation speeds, limited optical access, and multiphase nature of coolant flow in grinding present unique challenges that have so far hindered the use of such techniques for experimental validation of numerical models in this field.

To overcome these limitations, this study employs an integrated experimental–numerical approach for the quantitative validation of coolant flow simulations in grinding wheels. High-fidelity CFD models were developed for three internal channel inclination configurations: positive (aligned with the wheel rotation), straight (radial), and negative (against the wheel rotation), with operating parameters matched to the experimental setup. Transparent resin prototypes of the same designs were used to perform high-speed flow visualization and particle tracking, enabling direct validation of simulated velocities within the channels and qualitative assessment of jet formation at the outlets. By combining the spatial and temporal resolution of optical techniques with the predictive capacity of CFD, this approach bridges the gap between numerical modeling and real flow conditions inside rotating tools. Finally, grinding experiments under controlled conditions provided complementary thermal and mechanical performance data, allowing direct correlation between predicted flow behavior, observed coolant delivery patterns, and their actual impact on process efficiency.

2. Materials and methods

The main objective of this work was to experimentally validate CFD simulations of coolant flow in internally cooled grinding wheels and to correlate flow behavior with grinding performance. The study was designed under several constraints. First, the geometry of the channels had to match the nominal design used in the simulations, ensuring dimensional accuracy for direct comparison. Second, the prototypes had to be transparent to allow optical access for high-speed imaging and particle tracking. Third, the experimental setup needed to operate at

controlled flow rates and wheel speeds to replicate the simulation conditions, while ensuring stable illumination, minimal optical distortion, and repeatable acquisition conditions. Finally, the manufacturing and testing procedures had to be reproducible and cost-effective, enabling multiple tests with consistent results.

To meet these requirements, transparent resin grinding wheel replicas were produced by additive manufacturing for flow visualization, while vitrified alumina wheels were manufactured for grinding tests. The internal coolant delivery was evaluated using high-speed imaging and particle tracking on the transparent prototypes, and performance was assessed through grinding tests measuring forces and temperature. CFD simulations replicated the exact geometries and operating conditions of the experiments, enabling direct quantitative and qualitative validation.

2.1. Grinding wheel configurations

Three internal channel configurations were designed for the grinding wheels (Fig. 1): (a) positive inclination, channels inclined at $\theta = 12^{\circ}$ in the wheel rotation direction; (b) straight, radially aligned channels ($\theta = 0^{\circ}$); and (c) negative inclination, channels inclined at $\theta = 12^{\circ}$ opposite to the rotation direction. All geometries consisted of 30 channels with a nominal diameter of 1.7 mm, an external diameter of 62 mm, and an internal diameter of 21 mm. When assembling the grinding wheel, the passage is sealed on the side faces, ensuring that the fluid only exits through the channels.

Transparent resin prototypes (Fig. 1) were produced by additive manufacturing for flow visualization. The prototypes were fabricated using a 3D printer (Anycubic Photon D2, Anycubic, Shenzhen, China) employing Digital Light Processing (DLP) technology and Anycubic Clean translucent photopolymer resin. Printing parameters were set to a layer height of 50 μm, an exposure time of 2.4 s per layer, and 30 s for the base layers. After printing, the wheels were washed in isopropyl alcohol (≥ 95 % purity) for 5 min in an Anycubic Wash & Cure Plus unit, under continuous agitation, followed by internal channel cleaning with compressed air and complete drying. Post-curing was performed in the same unit under ultraviolet light ($\lambda = 405$ nm) for 6 min to ensure complete polymerization, improved mechanical strength and dimensional stability.

Surface finishing was obtained by mechanical polishing in a benchtop metallographic polisher, starting with manual sanding using 2000-grit silicon carbide paper, followed by a two-stage polishing sequence on cloth-covered rotating discs with abrasive suspensions. A lubricant fluid was also applied during polishing. This procedure yielded a translucent surface, enabling clear visualization of the particle-laden coolant flow inside the wheel during high-speed imaging experiments.

Alumina based wheels with vitrified bonds were manufactured in the same three inclinations for grinding tests. The abrasive mixture, composed of white alumina grains and a vitrified bond, was packed into steel molds together with a polymer structure (PLA) that defined the internal channel geometry. This polymer insert was produced by 3D printing and positioned in the mold prior to filling. The green bodies were pressed, dried, and subjected to the vitrification cycle, during which the polymer structure was burned out, leaving the open channels. After firing, the wheels were balanced and dressed before the grinding tests. Detailed information on the manufacturing process can be found in Costa et al. (2024) [50].

2.2. High-speed imaging and flow visualization

Flow visualization was performed using a CMOS Photron FASTCAM SA5 high-speed camera, recording 512 × 512 pixel sequences at 6000 fps with an exposure time of 1/100 000 s. The camera was positioned orthogonally to the wheel periphery, with the lens aligned to the central plane of the channels to minimize perspective distortion. Illumination was provided by a continuous halogen light source positioned in front of the wheel. To improve light uniformity and enhance particle visibility, a mirrored surface was fixed behind the resin wheel to reflect the light back through the channels.

A transparent resin replica of the grinding wheel was used to allow optical access to the internal channels. Plastic glitter particles (diameter = 0.4 mm) were dispersed in water and injected axially through the wheel spindle at a constant flow rate of 800 mL/min. This flow rate, higher than that used in the grinding tests (400 mL/min), was selected to improve visualization during high-speed recording. The wheel was driven at rotational speeds of 250, 2000, 3000, and 5000 rpm, and recordings were performed for each of the three grinding wheel configurations. The coolant reservoir containing the tracer particles was placed on a magnetic stirrer to promote uniform dispersion and prevent agglomeration. The experimental setup used for these measurements is shown in Fig. 2.

2.3. Particle tracking and velocity estimation

The displacement of particles inside the cooling channels was evaluated using two complementary approaches: manual and automatic tracking. The analysis was performed for the positive inclination channel geometry, as it exhibited the most uniform flow among the three configurations, and at a wheel speed of 250 rpm to facilitate controlled particle tracking.

In the manual method, a reference particle (p_1) was identified in the first frame (time t_1) and tracked until it approached the channel exit, reaching position p_1' at time t_2 (Figs. 3a and b). The corresponding images were corrected for wheel rotation, allowing the positions to be overlaid and aligned (Fig. 3c). The linear distance between p_1 and p_1' was measured with ImageJ software [51], and the particle velocity was

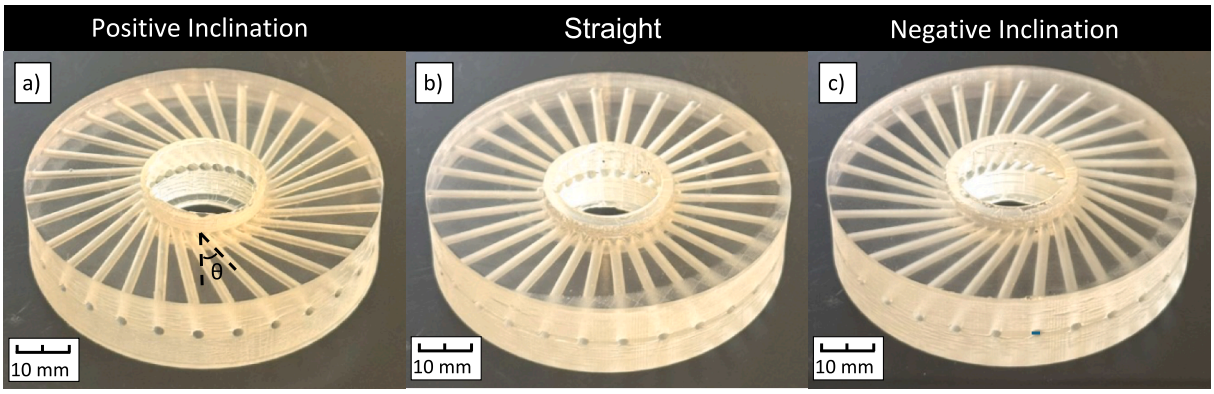

Fig. 1. Transparent resin prototypes of structured grinding wheels used for high-speed imaging and particle tracking: (a) positive inclination ($\theta = 12^{\circ}$ in the rotation direction); (b) straight ($\theta = 0^{\circ}$); and (c) negative inclination ($\theta = 12^{\circ}$ opposite to the rotation direction).

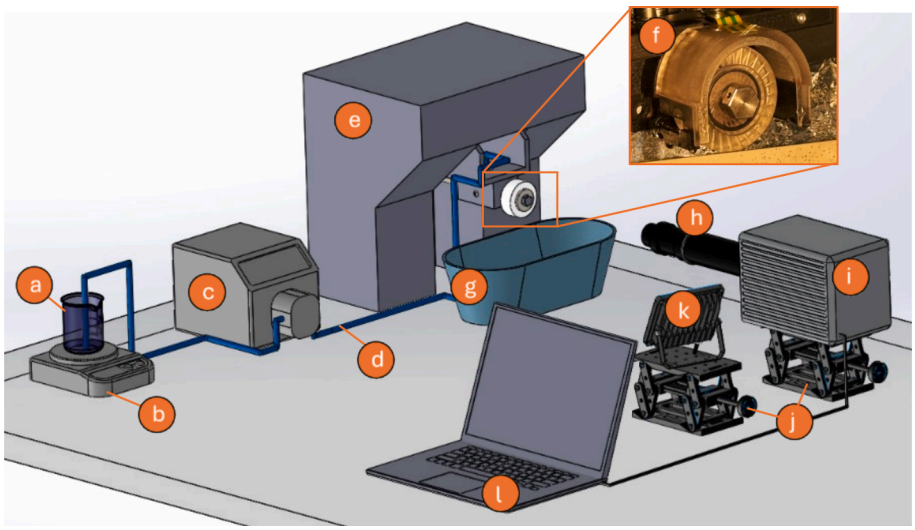

Fig. 2. Experimental setup for high-speed imaging: (a) coolant reservoir, (b) magnetic stirrer, (c) coolant pump, (d) supply pipe, (e) surface grinding machine, (f) resin grinding wheel, (g) reservoir for water collection, (h) optical lenses, (i) high-speed camera, (j) triaxial translation stage, (k) illumination system, and (l) computer for image acquisition and processing.

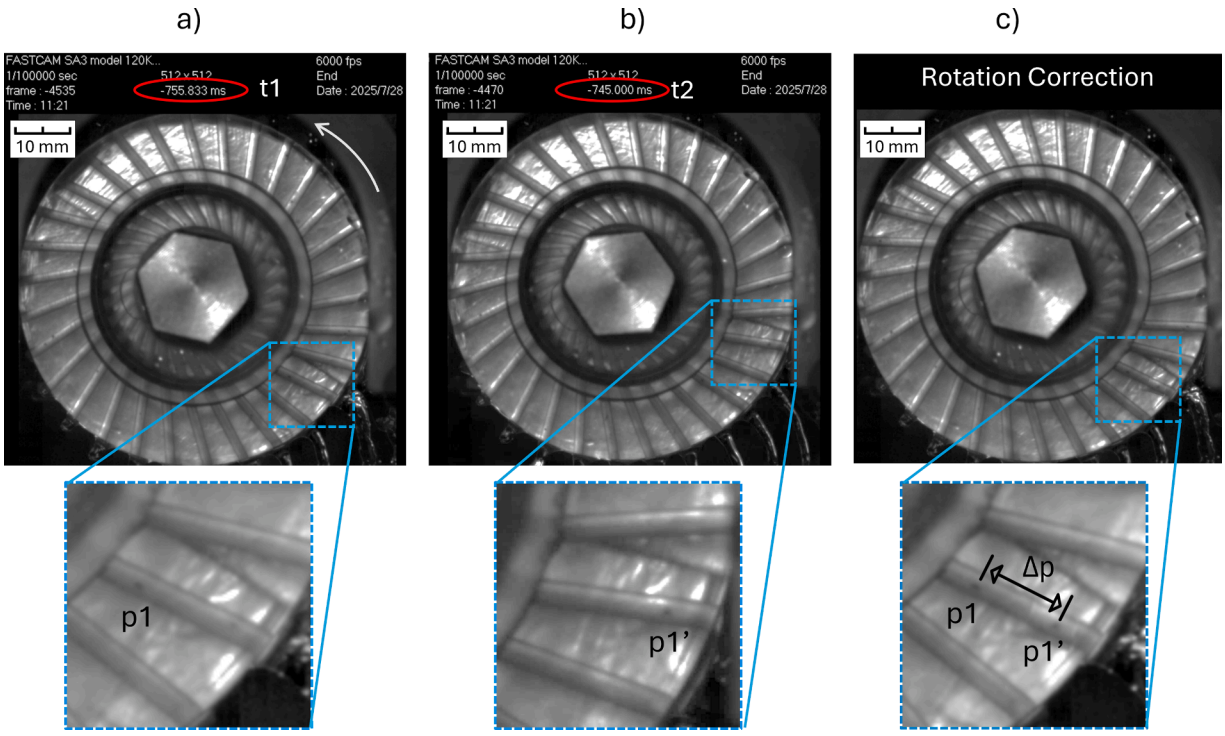

Fig. 3. Manual particle tracking method: (a) initial position of the reference particle (p_1) at time t_1; (b) final position (p_1') at time t_2; (c) rotation-corrected overlay of the two frames showing the measured displacement (Δp) used for velocity calculation.

calculated as:

$$v_{p1} = \frac{\Delta_p}{(t_2 - t_1)} \tag{1}$$

This procedure was repeated for 6 particles located in different channels of the grinding wheel, ensuring that the validation reflected the general flow behavior rather than a single-channel condition.

In the automatic method, raw images (923 frames; 512 × 512 px; Δt = 0.167 ms) were imported into Fiji/ImageJ 2 (ver. 1.54p) and rigidly aligned three times using *Linear Stack Alignment with SIFT* to eliminate rotation and micro-vibrations of the wheel. The contrast of each frame was normalized (*Enhance Contrast*, saturation = 0.4 %), and a static background was obtained by *Median Z-projection* and subtracted from the original stack (*Image Calculator* ▸ *Difference*), followed by Gaussian blur (σ = 1 px) to reduce noise. The analysis was restricted to the outer ring, isolated by combining two circular selections (*ROI Manager* ▸ *XOR*) and clearing the outside region (*Clear Outside*).

Tracking was performed in *TrackMate* v7.14 [52] using the LoG detector (estimated diameter = 0.4 mm; threshold = 2; sub-pixel on) and the *Simple LAP tracker* (linking = 0.5 mm; gap-closing = 0.5 mm; frame-gap = 2). Tracks with a duration < 10 frames or displacement < 3.11 mm were discarded, resulting in 32 valid particles. Instantaneous velocities (2D distance/Δt) were exported in XML format, converted to

Excel, and summarized as mean ± standard error for statistical analysis. The resulting trajectories were exported from TrackMate as an overlay image and imported into ImageJ. Each track was plotted as a line corresponding to the particle path, with the color scale representing the instantaneous velocity magnitude (blue = lowest, red = highest). This visualization allowed a qualitative assessment of the flow field and facilitated the identification of preferential flow regions within the wheel channels.

2.4. CFD simulation setup

The commercial software Ansys Fluent® was employed to solve the fluid flow problem. The computational domain was discretized using a hybrid strategy, combining tetrahedral elements in the shaft (0.4 mm) with structured hexahedral elements in the wheel center (0.28 mm, face sizing 0.18 mm) and in the cooling channels (0.18 mm). Inflation layers were applied to the channel walls, with a first layer thickness of 0.1 mm, six layers, and a growth rate of 1.2, to capture near-wall velocity gradients. A mesh-independence study was performed for the positive wheel configuration. The maximum outlet velocity at the channel aligned with gravity was monitored as the convergence criterion. As shown in Fig. 4b, coarse meshes produced overestimated velocities, while results stabilized when the mesh exceeded ~1.2 million elements. Beyond this threshold, variations were below 3 %, confirming grid independence. The final mesh of ~1.2 million elements (Fig. 4a) was adopted for all simulations, ensuring reliable accuracy while keeping computational requirements reasonable.

The velocity formulation was set *to Relative*, allowing the velocity field to be evaluated in the stationary reference frame while the wheel rotation was imposed via a Moving Reference Frame (MRF) [53–55]. Gravity was enabled ($y = -9.81$ m/s^2). Water was used as the working fluid, and several wheel rotation speeds were tested: 250 rpm for velocity validation via particle tracking, and 2000–5000 rpm for outlet velocity assessment. Due to resin shrinkage during the additive manufacturing process, the channel diameter of the resin prototypes decreased from the nominal 1.7 mm to 1.6 mm, therefore, the CFD model geometry was adjusted accordingly to allow direct comparison with the experimental particle-tracking results.

The governing equations solved were the continuity and momentum conservation equations for an incompressible Newtonian fluid [56–58]. The general form of the continuity equation is:

$$\frac{\partial \rho}{\partial t} + \nabla \bullet (\rho v) = 0 \tag{1}$$

For the present case, water at 20 °C was modeled as an incompressible fluid with constant density, so Eq. (1) reduces to:

$$\nabla \bullet (v) = 0 \tag{2}$$

The conservation of momentum is expressed as:

$$\rho\left(\frac{\partial v}{\partial t} + (v \bullet \nabla)v\right) = -\nabla p + \mu \nabla^2 v + \rho g \tag{3}$$

where v is the velocity vector, p is the static pressure ρ is the fluid density, μ is the dynamic viscosity, and g is the gravitational acceleration.

Boundary conditions included a mass flow inlet of 800 mL/min (0.01328 kg/s) at the wheel center, a pressure outlet with the *prevent reverse flow* option enabled [59], and stationary, no-slip walls. The solution method employed a coupled pressure–velocity scheme with *least squares cell-based* gradient evaluation and second-order discretization for pressure, momentum, and turbulence equations. A global time step was used for steady-state convergence. Based on the calculated Reynolds numbers (maximum ≈ 1980) [60], all simulated cases remained within the laminar flow regime; therefore, the laminar viscous model was employed throughout the simulations. When the external air domain is included, turbulence models such as k–ε (two-equation) are typically employed to capture the coolant–air interaction [28]. In the present case, since only the internal flow inside the channels was analyzed, the laminar model was deemed sufficient and physically consistent. The main physical and numerical parameters adopted in the CFD setup are summarized in Table 1.

From the simulation results, different velocity metrics were extracted depending on the intended comparison. For the simulations corresponding to the particle-tracking experiments, lines were created along the flow direction inside the channel domain, and the average velocity

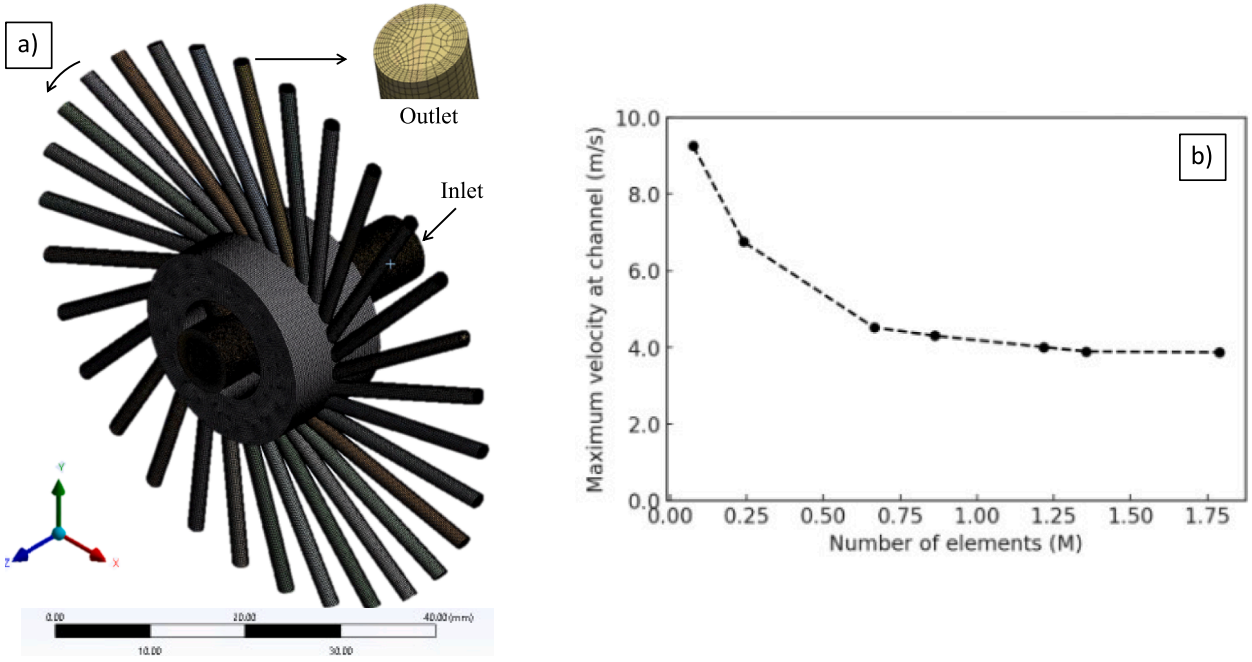

Fig. 4. Computational mesh and grid-independence study: (a) Final mesh adopted for the simulations, and (b) convergence of the maximum outlet velocity at the channel aligned with gravity for the positive wheel configuration.

Table 1
Summary of simulation parameters.

Parameter	Configuration
Fluid Properties	Water – Density: 998.2 kg/m^3; Viscosity: 1.00 × 10^{-3} kg/(m·s)
Velocity formulation	Relative
Flow Regime	Laminar
Rotation Method	Multiple Reference Frame (MRF); wheel center defined as rotating region; shaft and channels rotating consistently with this frame
Boundary Conditions	Inlet: Mass flow inlet at the shaft (800 mL/min) Outlet: Pressure outlet boundaries at all channel exits, with prevention of reverse flow enabled
Wall Treatment	No-slip
Numerical Scheme	Coupled pressure–velocity; least-squares cell-based gradient evaluation; second-order discretization for pressure and momentum
Gravity	Enabled
Convergence Criteria	Residuals < 10^{-4} and stable mass-flow balance

along these lines was calculated. This approach was adopted to approximate real flow conditions and to avoid the influence of near-wall zero-velocity regions. Additionally, velocity profiles were extracted on a cross-sectional plane within the channels, corresponding to the particle-tracking section, enabling direct comparison between simulated and experimental particle speeds. In the subsequent analyses, velocity contour plots were extracted at the channel outlets and a plane centered to the channels, and the average outlet velocity was computed for each configuration.

2.5. Grinding tests

The grinding tests were carried out in up-grinding mode on a surface grinding machine with a customized internal lubrication system. Three structured grinding wheels were tested, each operated at 5000 rpm (V_s = 16.23 m/s) with a table feed rate of 100 mm/min (V_w), at depths of cut of 10, 20, 50, 80 and 100 μm for three structured wheel geometries. Distilled water was fed axially through the spindle at 400 mL/min and delivered to the contact zone via internal cooling channels. This flow rate was selected based on previous work [28], where 400 mL/min proved sufficient to ensure effective temperature and force control under comparable grinding conditions, while higher values mainly resulted in unnecessary fluid consumption.

The workpieces were AISI 1045 steel (80 × 15 × 10 mm, 198 HV), pre-ground to ensure geometric and surface uniformity. The grinding wheels were dressed before each test using a multi-point diamond tool to restore the active cutting surface. All dressing operations were performed under identical conditions, and the grinding tests were repeated three times to ensure repeatability and, in particular, to minimize the influence of wheel surface topography on the measured forces and temperatures. Tangential and normal grinding forces were measured with a TAS3F load cell beneath the worktable (Fig. 5b), with a specified accuracy of ±0.3 %. Temperature was monitored using a K-type thermocouple embedded 1 mm below the workpiece surface and positioned at the mid-point of the track width, corresponding to 7.5 mm from both the track's start/end (Fig. 5d) at 5 Hz, with a measurement accuracy of ±1.5 °C. The temperature variation (ΔT) was calculated as the difference between the initial temperature at the start of the test and the maximum temperature recorded during grinding.

3. Results and Discussion

The results are organized to establish a direct connection between coolant flow behavior, as predicted by CFD, and its experimental verification through high-speed imaging and particle tracking, followed by the assessment of grinding performance. First, particle tracking data from transparent wheel prototypes are quantitatively compared with CFD predictions to validate simulated velocity fields inside the channels. Next, CFD results are extended to higher wheel speeds, examining the influence of channel inclination on outlet velocity magnitude and distribution. Flow visualization images complement this analysis by providing qualitative confirmation of jet coherence, direction, and

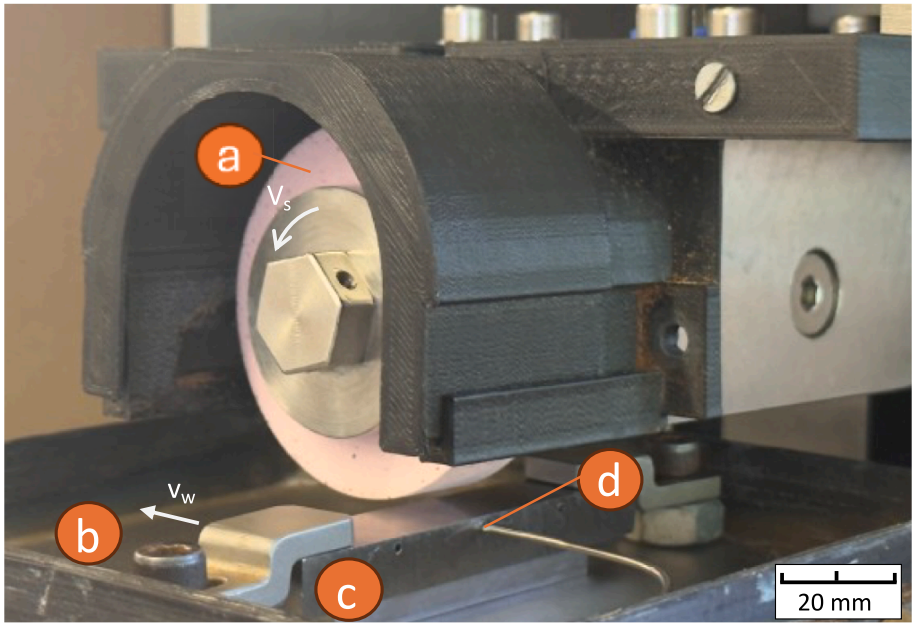

Fig. 5. Grinding experimental setup showing: (a) structured grinding wheel, (b) load cell positioned beneath the worktable, (c) workpiece, and (d) thermocouple position for temperature acquisition. Arrows indicate the grinding wheel peripheral speed (V_s) and table feed direction (V_w).

stability. Finally, grinding tests with vitrified alumina grinding wheels assess how these flow characteristics translate into temperature control and mechanical load variation reduction, enabling a direct correlation between internal channel design, coolant delivery efficiency, and overall process performance.

3.1. Experimental validation of CFD via particle velocity

Manual measurements were first performed on six individual particle trajectories to establish a baseline and serve as a reference for subsequent comparisons. Displacement was determined from the distance travelled between frames and the corresponding time interval. The resulting speeds ranged from 0.29 m/s to 0.56 m/s, with an average of 0.41 m/s and a standard deviation of 0.10 m/s (Table 2).

Fig. 6 compares the velocity field obtained by CFD simulation (a) with the particle trajectories extracted from high-speed videos using automatic tracking (b). Both approaches show a similar velocity range (0–0.6 m/s), reinforcing the agreement between the numerical predictions and the observed flow. While the overall structure is consistent in both cases, experimental trajectories occasionally display localized higher speeds, likely related to transient accelerations or particle movement through regions where the jet is redirected and accelerated. Optical distortions and overlapping trajectories may also lead to momentary overestimation of measured speeds. Nevertheless, the color distribution and trajectory alignment in both images indicate that the numerical model captures the main flow features inside the grinding wheel.

To complement this qualitative agreement, the mean velocities obtained from each method were compared quantitatively. For TrackMate, the value corresponds to the average speed of the 32 tracked particles, while in the CFD case it represents the average velocity along reference lines placed in the channel cross-section matching the particle-tracking location, ensuring direct comparability with the experimental results. Fig. 7 consolidates the results from the three evaluation methods: automatic tracking, manual measurements, and CFD simulation. The mean particle velocities from the experimental approaches were very close (0.40 m/s and 0.41 m/s), while the simulation yielded a slightly lower value (0.34 m/s). Despite the ~ 16 % difference, the three methods showed good agreement, validating the numerical model and demonstrating that the experimental particle-tracking method is effective for local flow characterization.

3.2. CFD analysis

Fig. 8 shows the evolution of the mean outlet fluid velocity as a function of the grinding wheel speed (V_s) for the three internal channel inclination configurations: negative, straight, and positive inclination. A monotonic increase in velocity is observed with increasing wheel rotation, although with different gradients. At 5000 rpm, for instance, the mean velocity in the positive inclination channels (1.05 m/s) is approximately twice that of the negative inclination channels (0.51 m/s), highlighting the strong influence of the channel geometry on the hydraulic performance.

The spatial distribution of velocity at the channel outlets further reinforces this effect. As shown in Fig. 9, increasing the wheel speed benefits all geometries, but both the magnitude and uniformity of velocity distribution vary significantly. Some configurations concentrate higher velocities in small portions of the outlet cross-section, while others display a more uniform pattern. In the negative-inclination case, even at high rotational speeds, the fluid exits remain confined to isolated and irregular regions within the outlet section, suggesting a fragmented and inefficient flow. The straight configuration exhibits a more coherent pattern: as the speed increases, the high-velocity band widens and becomes more evenly distributed across the outlet area, indicating better utilization of centrifugal energy. The positive inclination case shows the most pronounced effect: at 2000 rpm, well-defined high-velocity zones are already visible, and, at 5000 rpm the outlet cross-section is fully occupied by a continuous, uniform high-velocity region.

These results demonstrate not only the absolute increase in velocity with rotation, but also that the differences between geometries become more pronounced at higher speeds. At low speeds, certain sectors of comparable performance can still be observed among the three configurations; however, as V_s increases, the positive inclination channels stand out in both average velocity and, in the extent and uniformity of the high-velocity region, underlining the growing role of inclination in the hydraulic efficiency of the wheel.

A detailed view of the transition between the wheel hub and the internal channels reveals the mechanisms behind the superior performance of the positive inclination geometry (Fig. 10); the more favorable alignment between the channel axis and the direction of the centrifugal force promotes a smoother and more direct entry of the coolant into the channels. In contrast, in the straight and negative configurations the fluid trajectory appears less aligned with the channel axis, suggesting a less efficient transition. This qualitative difference explains why the positive inclination geometry achieves superior outlet velocities, as the optimized vector orientation and smoother hydrodynamic transition act synergistically to enhance fluid transport efficiency.

Additionally, to verify the effect of the dimensional deviation (0,1 mm change between simulation and experimental channel diameter), an extra simulation was performed for the positive-inclination wheel with the nominal 1.7 mm diameter channels, corresponding to the ceramic wheels used in the grinding tests. The outlet velocity differed by only −4% compared with the 1.6 mm case at 5000 rpm, confirming that the strong action of centrifugal force dominates the flow behavior, minimizing the influence of such a minor diameter variation.

3.3. Flow visualization using high-speed camera

High-speed imaging was used to capture the flow patterns for the three internal channel geometries tested at rotational speeds of 2000, 3000, and 5000 rpm (Fig. 11). The captured images reveal critical information about the coherence and orientation of the fluid jets and how these characteristics evolve with increasing rotational speed. Notably, more coherent jets (i.e., without breakage or significant deviation) occur predominantly in the positive and straight geometries at higher speeds, a behavior consistent with the higher outlet velocities observed in CFD simulations. This is essential for efficient fluid application, as high-velocity coolant jets are required to overcome the air barrier generated by wheel rotation, increase local hydrodynamic pressure, and promote effective penetration of the fluid into the contact zone [61].

In the negative inclination configuration, even at 5000 rpm, the jets remain thin, fragmented, and prone to lateral dispersion. Several channels exhibit reduced flow, indicating both lower ejection velocity and greater tangential deviation. This pattern suggests that the unfavorable channel orientation, opposite to the centrifugal force vector, limits fluid acceleration along the channel and hinders efficient projection.

For the straight configuration, jets become more continuous from 3000 rpm onwards, with well-defined streams over much of the outlet area at 5000 rpm. While performance is superior to the negative

Table 2
Manual measurements of particle displacement and speed from video frames.

Particle	Time (ms)	Displacement (mm)	Particle Speed (m/s)
P1	13.8	6.1	0.44
P2	13.8	7.7	0.56
P3	23.2	6.7	0.29
P4	25.3	8.0	0.32
P5	22.3	7.3	0.33
P6	13.8	7.1	0.51
Average (m/s)			0.41 ± 0.11
Std. Dev.			0.10

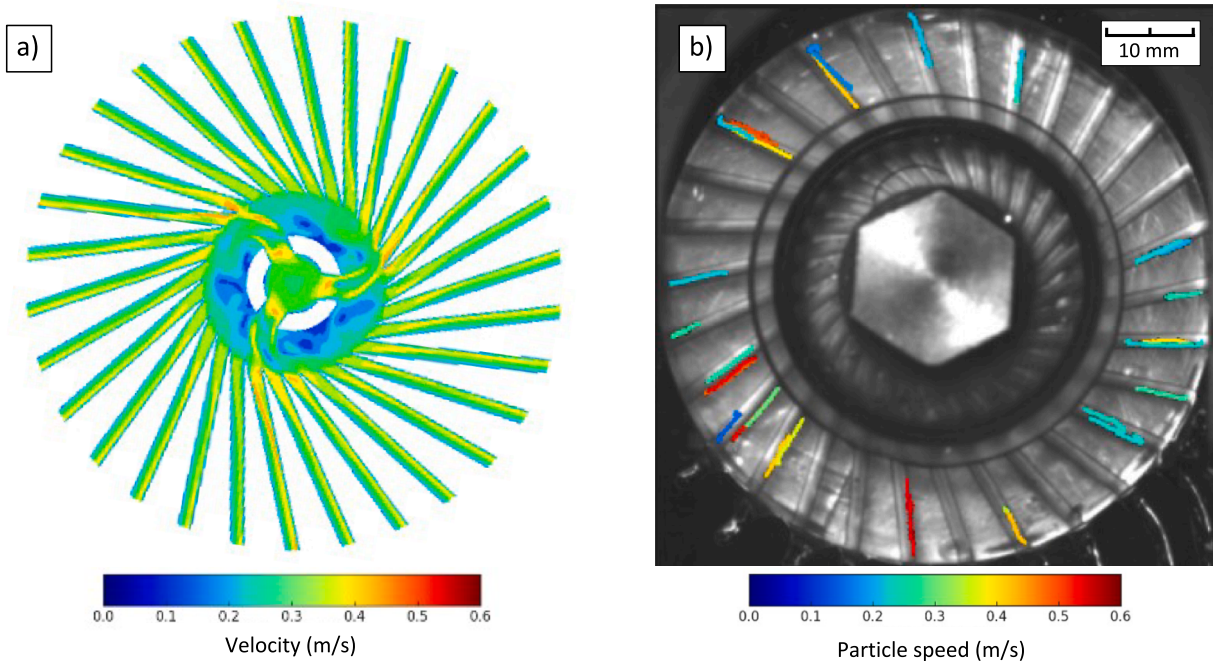

Fig. 6. (a) Fluid velocity field obtained by CFD simulation (positive inclination geometry, 250 rpm, 800 mL/min), and (b) particle trajectories tracked from high-speed videos using TrackMate. Colors represent local particle speed.

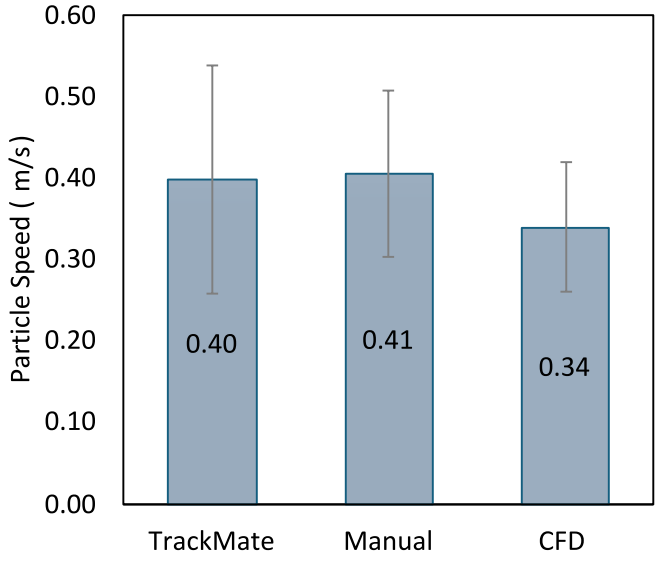

Fig. 7. Average particle speed obtained through automatic tracking (TrackMate), manual measurement, and CFD simulation. Error bars represent the standard deviation.

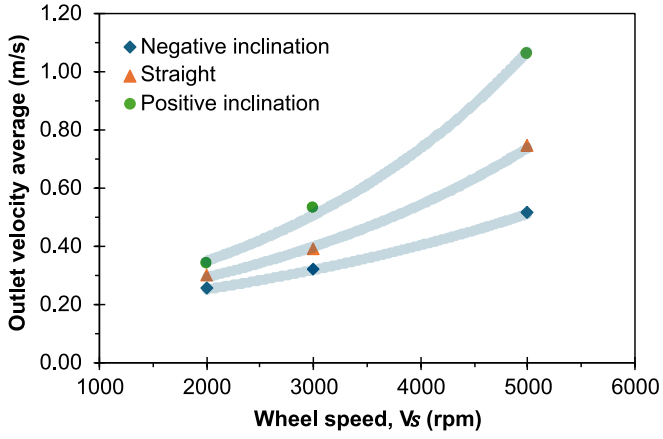

Fig. 8. Average outlet velocity as a function of wheel speed for three internal channel inclination geometries: negative, straight and positive.

inclination, occasional flow interruptions persist, which may compromise the uniformity of the fluid film on the workpiece and increase friction and tangential forces in zones without active lubricant coverage [62].

The positive inclination configuration demonstrates the most cohesive and stable pattern among the three geometries. At 3000 rpm, thick, continuous, and well-oriented jets are already visible; by 5000 rpm, the flow appears visually homogeneous in almost all channels, as highlighted by the magnified insets. The alignment of the channel axis with the centrifugal force vector enhances fluid acceleration and promotes a more radial, uniform ejection.

To quantify jet orientation, Fig. 12 presents the average inclination angles measured for the jet emerging from the channel most aligned with gravity (i.e., the one directly facing the workpiece under actual grinding conditions) at 5000 rpm. Values were obtained from 25 distinct, non-consecutive frames and represent the mean inclination of the coolant jet relative to the perpendicular to the workpiece surface.

The positive inclination geometry produced the lowest average angle (≈ 6.7°), indicating an almost perpendicular ejection toward the workpiece surface. This condition is advantageous for grinding, as it directs the jet with greater intensity into the contact zone, facilitating deeper and more effective penetration. The straight geometry showed an intermediate jet angle (≈ 30.0°), reflecting functional but less efficient hydraulic performance, while the negative inclination produced significantly larger deviations (≈ 41.2°), resulting in more tangential jets, reduced coolant delivery to the active zone, and increased lateral dispersion. Moreover, the standard deviation was higher in the negative inclination case (±5°), suggesting greater instability in jet behavior across the analyzed frames, consistent with the fragmentation and poor coherence observed in the high-speed images. In contrast, the straight and positive geometries showed lower deviations, indicating more

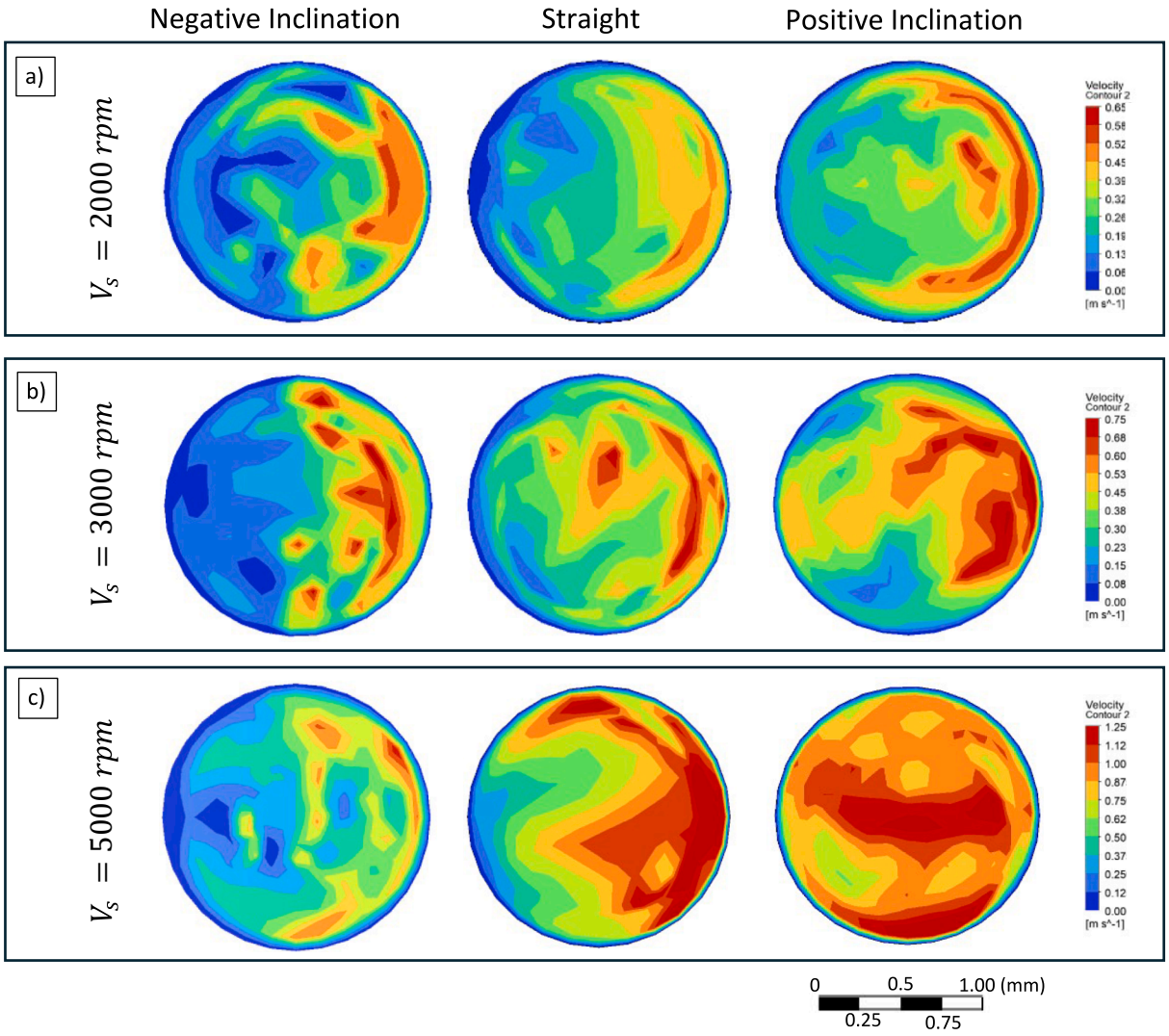

Fig. 9. Velocity contour maps at the channel outlets for grinding wheels with internal channels of negative inclination (left), straight (center) and positive inclination (right), with V_s at (a) 2000 rpm, (b) 3000 rpm and (c) 5000 rpm.

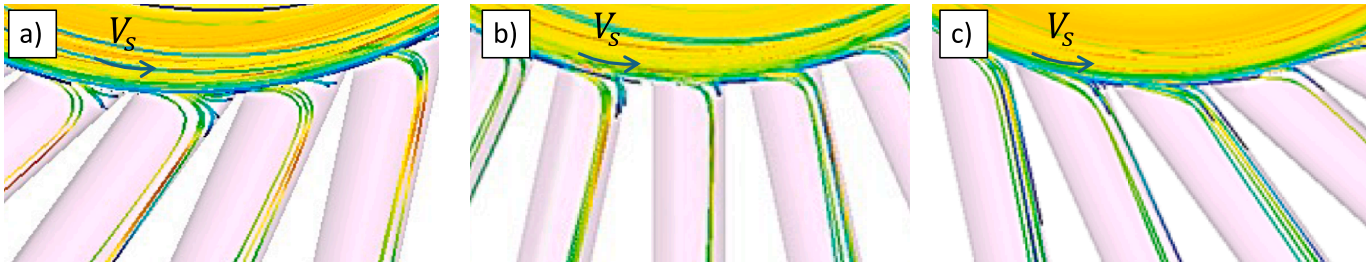

Fig. 10. Zoomed view of the streamline distribution at the transition between the wheel center and the channels, for the three internal cooling channel geometries: (a) negative inclination, (b) straight, and (c) positive inclination (5000 rpm).

repeatable and stable flow behavior at high speeds.

Overall, the high-speed camera recordings qualitatively confirm the CFD predictions presented in Section 3.2, particularly regarding jet outlet velocity. While the simulations provided average values and velocity vector fields for different geometries and speeds, the images reveal the practical manifestations of these velocities: thicker, continuous, and coherent jets appear only under the conditions where the simulations predict higher flow intensity. This direct correlation between numerically predicted velocity and the observed visual behavior reinforces the model's validity as a predictive tool for internal channel design. Minor discrepancies, such as the intermittent jet fragmentation seen in less favorable geometries, reflect transient free-surface phenomena not captured in the steady-state model but do not compromise the robustness of the overall trend. The good agreement between simulation and experiment in key parameters, jet intensity, orientation, and coverage, supports the practical use of CFD in developing more efficient internal lubrication solutions for grinding processes.

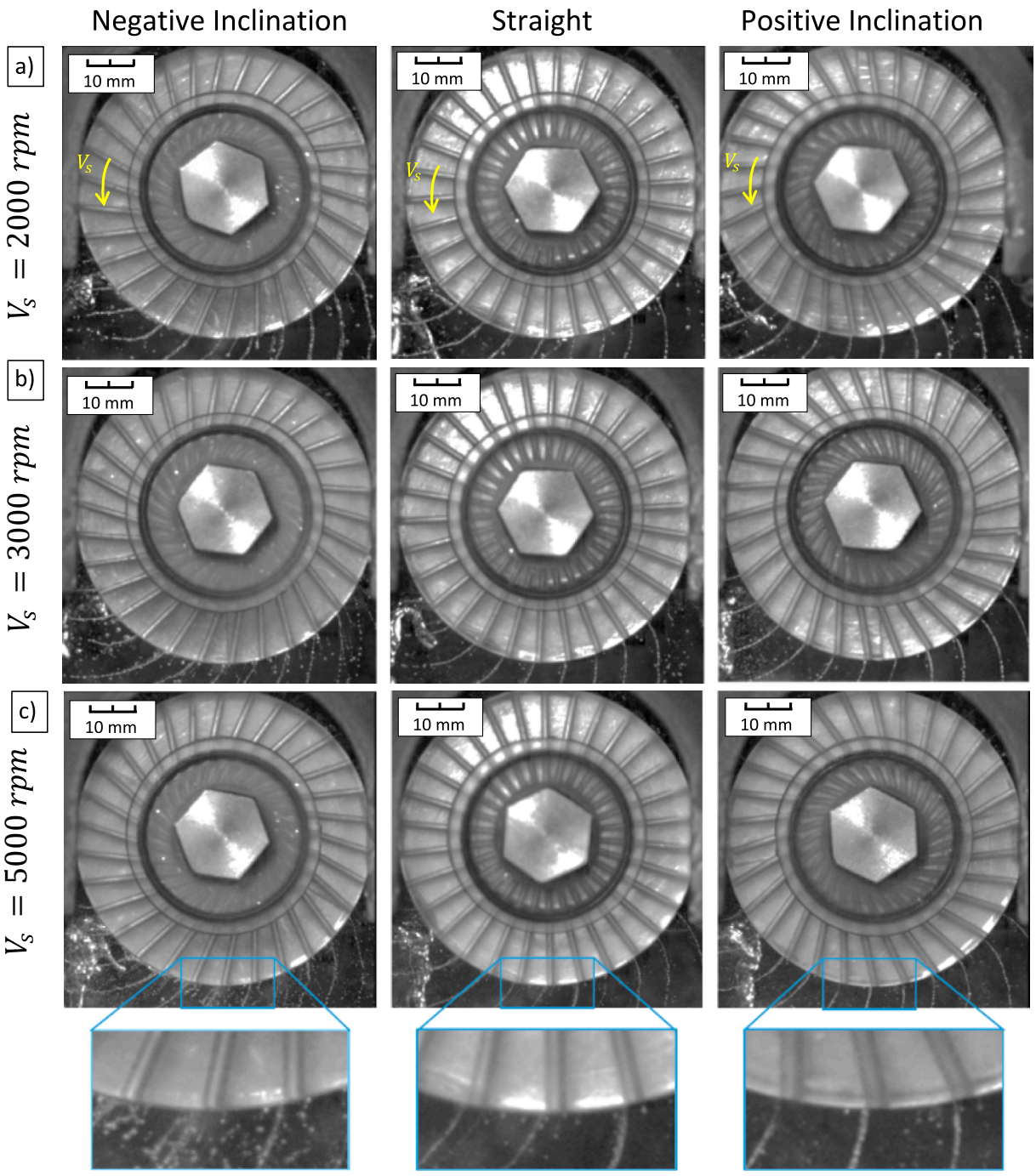

Fig. 11. High-speed images of fluid jets emerging from GW with three internal-channel geometries: negative (left column), straight (center) and positive inclination (right), at (a) 2000 rpm, (b) 3000 rpm and (c) 5000 rpm. Insets in (c) magnify the contact zone to highlight jet continuity at high rotation.

3.4. Grinding performance comparison

The experimental results allowed the evaluation of the impact of internal channel geometry on the thermal and mechanical performance of the grinding process. Three inclination configurations (positive, straight, and negative) were analyzed in terms of temperature variation in the contact zone, tangential forces, and normal ones.

The results show that the geometry of the internal channels plays a decisive role in process performance. The positive inclination configuration presented the most efficient and stable thermal behavior, recording a maximum temperature variation of only 9 °C at a depth of cut of 100 μm (Fig. 13a). This performance is associated with the favorable alignment of the channels with the centrifugal force vector, as discussed in previous sections, which promotes more effective fluid transport and delivery to the contact zone. In comparative terms, the positive inclination led to a 67 % reduction in temperature variation at 10 μm depth of cut, while for the other depths of cut the average reduction was 46 % compared to the negative inclination configuration.

For tangential forces (Fig. 13b), the positive inclination configuration achieved significant reductions at low and medium depths of cut. Up to 50 μm, tangential force was on average 50 % lower than in the negative inclination configuration, indicating more efficient material removal with less resistance to feed. Even at higher depths of cut, the positive configuration maintained the lowest tangential force levels, with an approximately linear trend across the entire range tested. The normal force results (Fig. 13c) show a similar pattern to the tangential

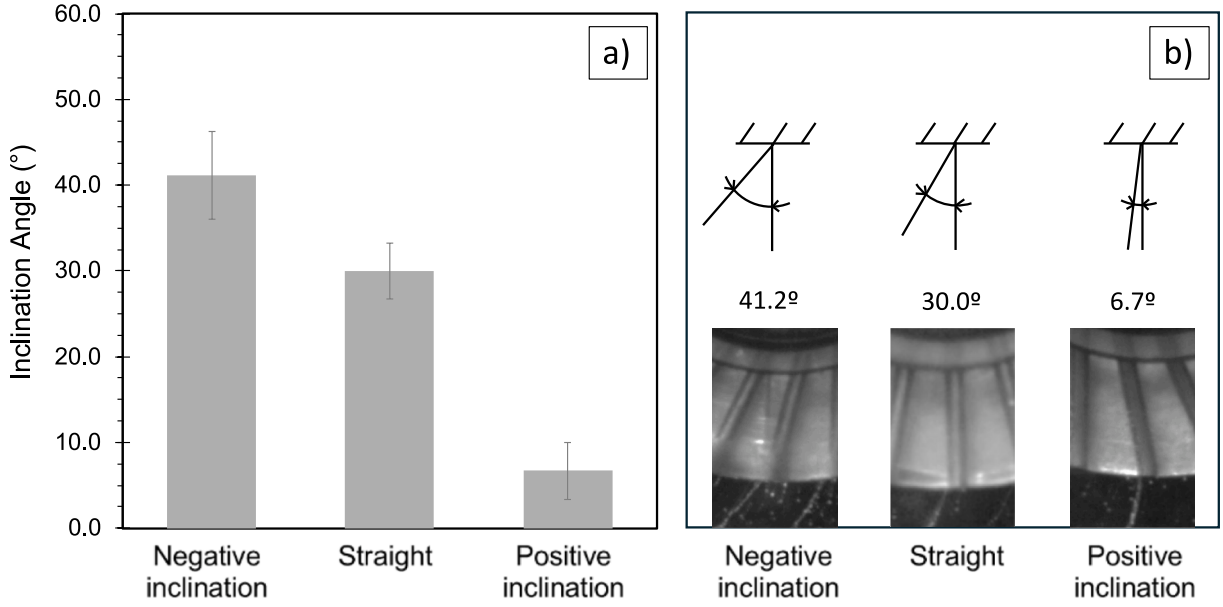

Fig. 12. (a) Average jet inclination angles at 5000 rpm for negative, straight, and positive channels, and (b) schematics and high-speed images showing mean jet angles of 41.2°, 30.0°, and 6.7°, respectively.

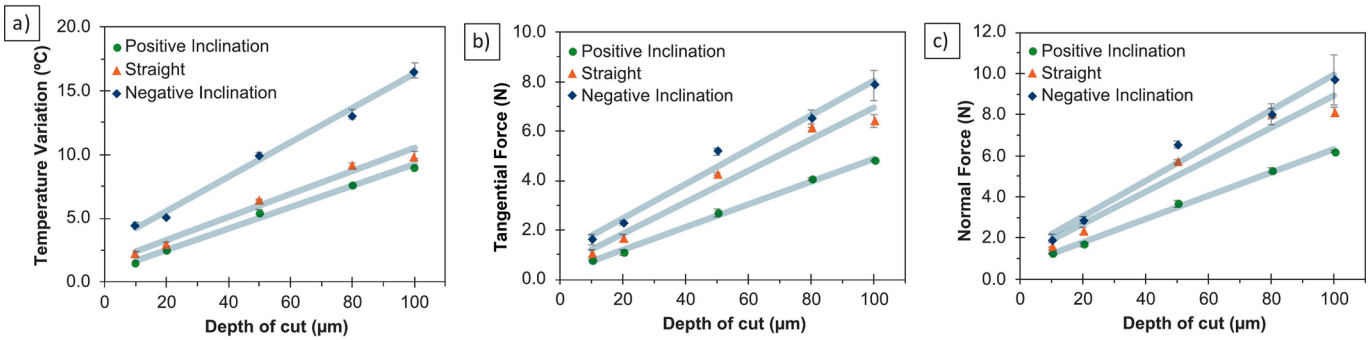

Fig. 13. Effect of channel inclination on grinding performance: (a) temperature, (b) tangential force, and (c) normal force as a function of depth of cut.

forces, with the positive inclination geometry presenting the lowest values across all tested depths of cut, achieving up to a 44 % reduction at 50 μm.

These experimental findings are consistent with the trends observed in the CFD simulation and flow visualization tests, strengthening the correlation between coolant delivery patterns and the thermal and mechanical behavior of the grinding process. The temperature and forces values obtained are consistent with those reported in the literature for comparable grinding conditions [63–66].

4. Conclusions

This work experimentally validated CFD predictions of coolant delivery in internally cooled grinding wheels with three channel inclinations (positive, straight, and negative) using high-speed imaging and particle tracking. The main conclusions are:

1. CFD–experiment agreement: Particle tracking results matched CFD predictions within a maximum deviation of 16 %, confirming the reliability of the numerical model for predicting coolant velocity in rotating channels.
2. Influence of channel inclination: Positive inclination channels produced the highest and most uniform outlet velocities, with jets nearly aligned to the centrifugal force, while negative inclination generated fragmented, tangential flows.
3. Flow visualization: High-speed imaging qualitatively confirmed the jet coherence and direction predicted by CFD, demonstrating the effectiveness of transparent resin prototypes for controlled flow visualization studies.
4. Grinding performance: Positive inclination channels reduced temperature rise by up to 67 %, normal forces by 44 %, and tangential forces by 50 %, consistently outperforming straight and negative inclinations across all tested depths of cut.
5. Practical implications: The methodology of combining CFD with targeted experiments is applicable to other rotating tools requiring efficient coolant delivery (e.g., milling cutters, drilling tools, cutting discs) and can be extended to different coolant types and viscosities, including oils, water–glycerin mixtures, MQL, and cryogenic fluids. It is also relevant for a wide range of material removal processes, from high-speed machining to micro-scale operations. This approach enables design optimization prior to manufacturing, reduces fluid consumption and environmental impact, and contributes to extending tool life in continuous industrial applications.

CRediT authorship contribution statement

Sharlane Costa: Writing – review & editing, Writing – original draft,

Visualization, Validation, Software, Investigation, Formal analysis, Data curation, Conceptualization. **Andrews Souza:** Writing – review & editing, Visualization, Validation, Methodology, Investigation, Conceptualization. **Lucas Neves:** Writing – review & editing, Formal analysis, Data curation. **João Ribeiro:** Writing – review & editing, Validation, Supervision, Project administration, Methodology, Funding acquisition, Formal analysis, Conceptualization. **Mário Pereira:** Writing – review & editing, Supervision, Methodology, Investigation, Formal analysis. **Delfim Soares:** Writing – review & editing, Supervision, Resources, Project administration, Investigation, Funding acquisition, Formal analysis, Conceptualization.

Declaration of competing interest

The authors declare that they have no known competing financial interests or personal relationships that could have appeared to influence the work reported in this paper.

Acknowledgements

This work was supported by FCT national funds, under the national support to R&D units grant, through the reference project UIDB/04436. The authors are grateful to the Foundation for Science and Technology (FCT, Portugal) for financial support through national funds FCT/MCTES (PIDDAC) to CIMO (UIDB/00690/2020 and UIDP/00690/2020) and SusTEC (LA/P/0007/2020). This work is within the scope of Sharlane Costa Ph.D. degree, in progress, financially supported by the Portuguese Foundation for Science and Technology (FCT) through the Ph.D grant reference 2021.07352.BD (DOI: https://doi.org/10.54499/2021.07352.BD). Andrews Souza was supported by FCT, under grant reference 2021.07961.BD (DOI: https://doi.org/10.54499/2021.07961.BD). Lucas B. Neves acknowledges the financial support from FCT through the doctoral grant 2025.00900.BDANA.

Data availability

No data was used for the research described in the article.

References

[1] A.K. Singh, A. Kumar, V. Sharma, P. Kala, Sustainable techniques in grinding: State of the art review, J. Clean. Prod. 269 (2020) 121876, https://doi.org/10.1016/j.jclepro.2020.121876.
[2] P. Capela, S. Costa, M.S. Souza, S. Carvalho, M. Pereira, L. Carvalho, J.R. Gomes, D. Soares, Wear behavior of a new composite formulation, with TEOS addition, for abrasive vitrified grinding wheels, Wear 512–513 (2023) 204524, https://doi.org/10.1016/J.WEAR.2022.204524.
[3] Y. Luo, W. Liao, W. Tang, X. Wang, C. Mao, M. Zhang, K. Tang, W. Wang, B. Cheng, A. Razzak, Theoretical and experimental analysis of temperature distribution in variable-depth reciprocating grinding process, J. Manuf. Process. 151 (2025) 89–102, https://doi.org/10.1016/J.JMAPRO.2025.07.014.
[4] P. Zhao, B. Lin, J. Zhou, B. Lv, J. Li, J. Zhang, L. Wang, T. Sui, Review of grinding temperature theory and measurement for the needs of the times: Promoting the development of advanced manufacturing, J. Mater. Process. Technol. 337 (2025) 118744, https://doi.org/10.1016/J.JMATPROTEC.2025.118744.
[5] D.Y. Pimenov, L.R. Ribeiro da Silva, M. Kuntoğlu, B.S. Abrão, L.E. dos Santos Paes, E. Linul, Review of advanced sensor system applications in grinding operations, J. Adv. Res. (2025), https://doi.org/10.1016/j.jare.2025.01.013.
[6] J.Z. Zhang, X.M. Tan, B. Liu, X.D. Zhu, Investigation for convective heat transfer on grinding work-piece surface subjected to an impinging jet, Appl. Therm. Eng. 51 (2013) 653–661, https://doi.org/10.1016/J.APPLTHERMALENG.2012.10.011.
[7] E. García, D. Méresse, I. Pombo, S. Harmand, J.A. Sánchez, Identification of heat partition in grinding related to process parameters, using the inverse heat flux conduction model, Appl. Therm. Eng. 66 (2014) 122–130, https://doi.org/10.1016/J.APPLTHERMALENG.2014.01.048.
[8] M. Gostimirovic, M. Sekulic, M. Trifunovic, M. Madic, D. Rodic, Stability analysis of the inverse heat transfer problem in the optimization of the machining process, Appl. Therm. Eng. 195 (2021) 117174, https://doi.org/10.1016/J.APPLTHERMALENG.2021.117174.
[9] I. Deiab, S.W. Raza, S. Pervaiz, Analysis of Lubrication strategies for Sustainable Machining during Turning of Titanium Ti-6Al-4V Alloy, Procedia CIRP 17 (2014) 766–771, https://doi.org/10.1016/J.PROCIR.2014.01.112.
[10] Y. Zhang, J.A. Robles-Linares, L. Chen, Z. Liao, A.J. Shih, C. Wang, Advances in machining of hard tissues – from material removal mechanisms to tooling solutions, Int. J. Mach. Tools Manuf 172 (2022) 103838, https://doi.org/10.1016/J.IJMACHTOOLS.2021.103838.
[11] N. Qian, F. Jiang, M. Marengo, J. Chen, Y. Fu, J. Zhang, J. Xu, Start-up behavior of oscillating heat pipe in grinding wheel under axial-rotation conditions, Appl. Therm. Eng. 219 (2023) 119443, https://doi.org/10.1016/J.APPLTHERMALENG.2022.119443.
[12] A. Bagherzadeh, F. Pashmforoush, H. Jamshidi, E. Budak, Fundamentals of cooling/lubrication effect in grinding of Inconel 718 employing an inverse thermo-mechanical model, Tribol. Int. 209 (2025) 110746, https://doi.org/10.1016/J.TRIBOINT.2025.110746.
[13] A.V. de Mello, R.B. de Silva, Á.R. Machado, R.V. Gelamo, A.E. Diniz, R.F.M. de Oliveira, Surface Grinding of Ti-6Al-4V Alloy with SiC Abrasive Wheel at Various cutting Conditions, Procedia Manuf. 10 (2017) 590–600, https://doi.org/10.1016/J.PROMFG.2017.07.057.
[14] B. Espenhahn, L. Schumski, D. Meyer, D. Stöbener, A. Fischer, Optical measurement approach to analyse the tool-workpiece interacting flow of grinding processes, Flow Meas. Instrum. 93 (2023) 102407, https://doi.org/10.1016/j.flowmeasinst.2023.102407.
[15] S. Li, M. Ou, W. Cai, J. Li, Q. Xiao, M. Zou, Effect of pores on the performance of diamond grinding wheels fabricated by laser additive manufacturing, Wear 572–573 (2025) 206019, https://doi.org/10.1016/J.WEAR.2025.206019.
[16] K. Jayakumar, Effect of grinding parameters and coolants on grindability of Ti grade 9 alloy, Mater. Today Proc. (2024), https://doi.org/10.1016/j.matpr.2024.04.030.
[17] E. Brinksmeier, C. Heinzel, M. Wittmann, Friction, Cooling and Lubrication in Grinding, CIRP Ann. 48 (1999) 581–598, https://doi.org/10.1016/S0007-8506(07)63236-3.
[18] A. Basem, M. Naji, H.A. Al-Asadi, M. Sediq Safi, G. Daminova, M. Alhadrawi, M. J. Alfaker, S. Islam, Small-quantity cooling lubrication in creep-feed grinding: Surface quality and residual stress analysis, Results Eng. 22 (2024) 102348, https://doi.org/10.1177/09544054221147622.
[19] N. Qian, F. Jiang, M. Marengo, Y. Fu, J. Xu, Thermal performance of a radial-rotating oscillating heat pipe and its application in grinding processes with enhanced heat transfer, Appl. Therm. Eng. 233 (2023) 121213, https://doi.org/10.1016/J.APPLTHERMALENG.2023.121213.
[20] M. Sarikaya, M.K. Gupta, I. Tomaz, M. Danish, M. Mia, S. Rubaiee, M. Jamil, D. Y. Pimenov, N. Khanna, Cooling techniques to improve the machinability and sustainability of light-weight alloys: a state-of-the-art review, J. Manuf. Process. 62 (2021) 179–201, https://doi.org/10.1016/J.JMAPRO.2020.12.013.
[21] J. Chen, Y. Fu, Q. He, H. Shen, C.Y. Ching, D. Ewing, Environmentally friendly machining with a revolving heat pipe grinding wheel, Appl. Therm. Eng. 107 (2016) 719–727, https://doi.org/10.1016/J.APPLTHERMALENG.2016.07.030.
[22] L. Zhao, R. Peng, J. Gao, Y. Li, M. Chen, Mechanistic design of porous self-lubricating grinding wheels with integrated internal cooling: Role of PMMA and nickel-coated MoS_2 composites in machining enhancement, J. Mater. Process. Technol. 340 (2025) 118877, https://doi.org/10.1016/J.JMATPROTEC.2025.118877.
[23] X. Li, Z. Chen, W. Chen, Suppression of Surface Burn in Grinding of Titanium Alloy TC4 using a Self-inhaling Internal Cooling Wheel, Chin. J. Aeronaut. 24 (2011) 96–101, https://doi.org/10.1016/S1000-9361(11)60012-5.
[24] X. Xiao, B. Li, R. Peng, X. Hao, X. Huang, Y. Li, L. Zhao, M. Chen, J. Gao, Analysis of the material removal and heat transfer during internal cooling grinding of GH4169, J. Mater. Process. Technol. 322 (2023) 118199, https://doi.org/10.1016/J.JMATPROTEC.2023.118199.
[25] R. Peng, W. Yan, L. Zhao, M. Chen, X. Xiao, Design and performance evaluation of a directional internal-cooling grooved grinding wheel with optimized coolant supply structure, J. Manuf. Process. 141 (2025) 155–168, https://doi.org/10.1016/J.JMAPRO.2025.02.059.
[26] J. Sieniawski, K. Nadolny, Experimental study into the grinding force in surface grinding of steel CrV12 utilizing a zonal centrifugal coolant provision system, Proc. Inst. Mech. Eng. B J. Eng. Manuf. 232 (2016) 394–403, https://doi.org/10.1177/0954405416645256.
[27] S. Costa, M. Pereira, J. Ribeiro, D. Soares, Texturing Methods of Abrasive Grinding Wheels: a Systematic Review, Materials 15 (2022) 8044, https://doi.org/10.3390/ma15228044.
[28] S. Costa, P. Capela, A. Hassui, J. Ribeiro, M. Pereira, D. Soares, CFD analysis of multi-layer cooling channels in three-dimensionally structured grinding wheels, Appl. Therm. Eng. 279 (2025) 127633, https://doi.org/10.1016/j.applthermaleng.2025.127633.
[29] R. Peng, L. Zhao, J. Tong, M. Chen, M. Zhou, A. Li, Design and evaluation of an internal-cooling grooved grinding wheel, J. Manuf. Process. 73 (2022) 1–16, https://doi.org/10.1016/J.JMAPRO.2021.10.061.
[30] J. Sieniawski, K. Nadolny, The effect upon grinding fluid demand and workpiece quality when an innovative zonal centrifugal provision method is implemented in the surface grinding of steel CrV12, J. Clean. Prod. 113 (2016) 960–972, https://doi.org/10.1016/J.JCLEPRO.2015.11.017.
[31] X. Xiao, Y. Jin, M. Chen, R. Peng, H. Tang, J. Gao, An internal cooling grinding wheel: from design to application, Chin. J. Aeronaut. 36 (2023) 465–482, https://doi.org/10.1016/J.CJA.2023.02.024.
[32] A.-M.-O. Mohamed, R. Bauer, A. Warkentin, Uncut chip thickness and coolant delivery effects on the performance of circumferentially grooved grinding wheels, Int. J. Adv. Manuf. Technol. 85 (2016) 1429–1438, https://doi.org/10.1007/s00170-015-8062-6.
[33] J.C. Lopes, A.G. Talon, M. de S. Rodrigues, G.B. Moretti, F. de C. Machado, G.G. de Souza, F.S.F. Ribeiro, L.E. de A. Sanchez, E.C. Bianchi, An experimental evaluation between pure and diluted MQL versus flood lubri-cooling focused on

cost and environmental impact, The International Journal of Advanced Manufacturing Technology 129 (2023) 2691–2705, https://doi.org/10.1007/s00170-023-12399-6.
[34] K. Kishore, S.R. Chauhan, M. Kumar Sinha, A comprehensive investigation on eco-benign grindability improvement of Inconel 625 using nano-MQL, Precis. Eng. 90 (2024) 81–95, https://doi.org/10.1016/J.PRECISIONENG.2024.08.004.
[35] F. Abedrabbo, A. Madariaga, D. Soriano, M. Pérez, E. Butano, R. Fernández, S. Abolghasem, P.J. Arrazola, Influence of cryogenic grinding surface on fatigue performance of carburised 27MnCr5, J. Mater. Res. Technol. 23 (2023) 1792–1804, https://doi.org/10.1016/J.JMRT.2023.01.111.
[36] M. Chen, R. Peng, A. Li, X. Xiao, L. Zhao, Assessment of surface structure optimization in internal cooling grinding, Int. J. Adv. Manuf. Technol. 123 (2022) 2139–2155, https://doi.org/10.1007/s00170-022-10304-1.
[37] M. Dogra, V.S. Sharma, J.S. Dureja, S.S. Gill, Environment-friendly technological advancements to enhance the sustainability in surface grinding- a review, J. Clean. Prod. 197 (2018) 218–231, https://doi.org/10.1016/J.JCLEPRO.2018.05.280.
[38] M. Hadad, An experimental investigation of the effects of machining parameters on environmentally friendly grinding process, J. Clean. Prod. 108 (2015) 217–231, https://doi.org/10.1016/J.JCLEPRO.2015.05.092.
[39] A. Elsheikh, A.B.M. Ali, A. Saba, H. Faqeha, A.A. Alsaati, A.M. Maghfuri, W. Abd-Elaziem, A.A. El Ashmawy, N. Ma, A review on sustainable machining: Technological advancements, health and safety considerations, and related environmental impacts, Results Eng. 24 (2024) 103042, https://doi.org/10.1016/J.RINENG.2024.103042.
[40] B. Zhao, X. Wang, T. Chen, W. Ding, N. Qian, J. Xu, Simulation and experimental thermal analysis of ultrasonic vibration-assisted high-efficiency deep grinding of γ-TiAl blade tenon, Appl. Therm. Eng. 258 (2025) 124629, https://doi.org/10.1016/J.APPLTHERMALENG.2024.124629.
[41] M. Li, Y. Huang, W. Wang, H. Li, S. Yan, L. Zou, Enhanced heat transfer in 3D printed ball-end grinding tool with blade-shaped structure, Appl. Therm. Eng. 244 (2024) 122760, https://doi.org/10.1016/J.APPLTHERMALENG.2024.122760.
[42] H. Yu, K. Sun, W. Ren, J. Zhang, Z. Han, Synergistic improvement of grinding fluid utilization and workpiece surface quality using combinatorial bionic structured grinding wheels, J. Manuf. Process. 130 (2024) 102–117, https://doi.org/10.1016/J.JMAPRO.2024.08.046.
[43] S.B. Thekkoot Surendran, V.S. Sooraj, Enhancing useful flow of cutting fluid and thermal performance in surface grinding via segmented wheel, Mater. Today Proc. 90 (2023) 208–213, https://doi.org/10.1016/J.MATPR.2023.06.090.
[44] L. Zhao, R. Peng, J. Gao, Y. Li, X. Tang, X. Chen, Z. Tan, Synergistic Nanofluids-Porous self-lubricating Internal Cooling Wheel for Superalloy Grinding, Int. J. Mech. Sci. 302 (2025) 110576, https://doi.org/10.1016/J.IJMECSCI.2025.110576.
[45] Z. Wang, J. Li, Q. Liu, L. Chen, J. Lv, T. Yu, J. Zhao, No-impact trajectory design and fabrication of surface structured CBN grinding wheel by laser cladding remelting method, Opt. Laser Technol. 181 (2025) 111956, https://doi.org/10.1016/J.OPTLASTEC.2024.111956.
[46] Y. Saffar, M. Kulka, D.S. Nobes, R. Sabbagh, Simultaneous circulating tumor cells (CTCs) tracking and flow field characterization through integrated single camera imaging in a micro-hydrocyclone, Chem. Eng. J. 520 (2025) 165681, https://doi.org/10.1016/J.CEJ.2025.165681.
[47] S. Salavatidezfouli, S. Barzegar, A. Sheidani, A. Hajisharifi, M. Girfoglio, G. Stabile, G. Rozza, Effect of particle aspect ratio in targeted drug delivery in abdominal aortic aneurysm, Eur. J. Mech. B. Fluids 106 (2024) 181–196, https://doi.org/10.1016/J.EUROMECHFLU.2024.04.009.
[48] E.J. Carboni, B.H. Bognet, G.M. Bouchillon, A.L. Kadilak, L.M. Shor, M.D. Ward, A. W.K. Ma, Direct Tracking of Particles and Quantification of Margination in Blood Flow, Biophys. J . 111 (2016) 1487–1495, https://doi.org/10.1016/J.BPJ.2016.08.026.
[49] O.A. Sindeeva, Z.V. Kozyreva, A.S. Abdurashitov, G.B. Sukhorukov, Engineering colloidal systems for cell manipulation, delivery, and tracking, Adv. Colloid Interface Sci. 340 (2025) 103462, https://doi.org/10.1016/J.CIS.2025.103462.
[50] S. Costa, P. Capela, M.S. Souza, J.R. Gomes, L. Carvalho, M. Pereira, D. Soares, A New Grinding Wheel Design with a 3D Internal Cooling Structure System, Journal of Manufacturing and Materials Processing 8 (2024) 159, https://doi.org/10.3390/jmmp8040159.
[51] C.A. Schneider, W.S. Rasband, K.W. Eliceiri, NIH image to ImageJ: 25 years of image analysis, Nat. Methods 9 (2012) 671–675, https://doi.org/10.1038/nmeth.2089.
[52] D. Ershov, M.-S. Phan, J.W. Pylvänäinen, S.U. Rigaud, L. Le Blanc, A. Charles-Orszag, J.R.W. Conway, R.F. Laine, N.H. Roy, D. Bonazzi, G. Duménil, G. Jacquemet, J.-Y. Tinevez, TrackMate 7: integrating state-of-the-art segmentation algorithms into tracking pipelines, Nat. Methods 19 (2022) 829–832, https://doi.org/10.1038/s41592-022-01507-1.
[53] M. Rasouli, S.M. Mousavi, H. Azargoshasb, O. Jamialahmadi, Y. Ajabshirchi, CFD simulation of fluid flow in a novel prototype radial mixed plug-flow reactor, J. Ind. Eng. Chem. 64 (2018) 124–133, https://doi.org/10.1016/J.JIEC.2018.03.008.
[54] A. Reid, R. Rossi, C. Cottini, A. Benassi, CFD simulation of a Rushton turbine stirred-tank using open-source software with critical evaluation of MRF-based rotation modeling, Meccanica 60 (2025) 1613–1637, https://doi.org/10.1007/s11012-024-01824-z.
[55] R.K. Agarwal, J.E. Deese, Euler calculations for flowfield of a helicopter rotor in hover, J. Aircr. 24 (1987) 231–238, https://doi.org/10.2514/3.45431.
[56] H.K. Versteeg, An introduction to computational fluid dynamics the finite volume method, 2/E, Pearson Education India, 2007.
[57] G.K. Batchelor, An introduction to fluid dynamics, Cambridge University Press, 2000.
[58] P.G. Zadeh, J.D. Chung, Efficiency and performance evaluation of a novel EV Air-conditioning and battery cooling system with desiccant-coated heat pump, Appl. Therm. Eng. 264 (2025) 125429, https://doi.org/10.1016/J.APPLTHERMALENG.2025.125429.
[59] M.A.A. Bin Ishak, A. Ibrahim, S.I.U. Din, Energy and exergy analysis of a reversed circular flow jet impingement bifacial PVT collector: CFD simulation and experimental study, Therm. Sci. Eng. Prog. 62 (2025) 103602, https://doi.org/10.1016/J.TSEP.2025.103602.
[60] L. Hu, C. Pan, D. Hu, H. Yan, F. Qiu, Z. Cheng, Coupled CFD-machine learning optimization of inlet water-jet orifices in jet impact negative pressure reactors, J. Taiwan Inst. Chem. Eng. 175 (2025) 106248, https://doi.org/10.1016/J.JTICE.2025.106248.
[61] A. Vesali, T. Tawakoli, Study on Hydrodynamic pressure in Grinding Contact Zone considering Grinding Parameters and Grinding Wheel specifications, Procedia CIRP 14 (2014) 13–18, https://doi.org/10.1016/J.PROCIR.2014.03.053.
[62] K. Nadolny, Small-dimensional sandwich grinding wheels with a centrifugal coolant provision system for traverse internal cylindrical grinding of steel 100Cr6, J. Clean. Prod. 93 (2015) 354–363, https://doi.org/10.1016/J.JCLEPRO.2015.01.046.
[63] S.K. Tamil Vanan, E.U. Olugu, C.K. Ang, S.A. Lawal, O.C. Aja, Evaluation of surface grinding of AISI 304 stainless steel using dry and compressed air cooling techniques, SN Appl Sci 3 (2021) 389. doi: 10.1007/s42452-021-04395-w.
[64] P. Morsch, J. Kühn, R. Werner, H. Anlauf, D.U. Geier, T. Becker, H. Nirschl, Influence of the filter cloth and nozzles type on the in-situ cleaning procedure of filter presses, Chem. Eng. Sci. 226 (2020) 115889, https://doi.org/10.1016/J.CES.2020.115889.
[65] S. Majumdar, P. Das, S. Kumar, D. Roy, S. Chakraborty, Evaluation of cutting fluid application in surface grinding, Measurement 169 (2021) 108464, https://doi.org/10.1016/J.MEASUREMENT.2020.108464.
[66] M. Barmouz, B. Azarhoushang, Additive manufacturing of hybrid bond grinding wheels via digital light processing: Performance enhancement through composition alteration and groove incorporation, Results Eng. 27 (2025) 105808, https://doi.org/10.1016/J.RINENG.2025.105808.